Title

Dual-Gradient Construction on Li-rich Cathodes for High Stability Lithium Battery

*Tianhao Wu, Xu Zhang, Shiqi Liu, Zengqing Zhuo, Wanli Yang, Lingqiao Wu, Dongdong Xiao, and Haijun Yu**

T. Wu, Prof. X. Zhang, Dr. L. Wu, S. Liu, Prof. H. Yu

Institute of Advanced Battery Materials and Devices

College of Materials Science and Engineering

Beijing University of Technology

Beijing 100124, China

E-mail: hj-yu@bjut.edu.cn

T. Wu, Prof. X. Zhang, Dr. L. Wu, S. Liu, Prof. H. Yu

Key Laboratory of Advanced Functional Materials

Ministry of Education

Beijing University of Technology

Beijing 100124, P. R. China

T. Wu, Prof. X. Zhang, Dr. L. Wu, S. Liu, Prof. H. Yu

Institute of Matter Science

Beijing University of Technology

Beijing 100124, China

Prof. W. Yang, Z. Zhuo

Advanced Light Source

Lawrence Berkeley National Laboratory

Berkeley CA 94720, USA

Prof. D. Xiao

Beijing National Laboratory for Condensed Matter Physics

Institute of Physics, Chinese Academy of Sciences

Beijing 100190, P. R. China

Keywords: Li-rich layered oxides, dual-gradient construction, gradient Al/Mg co-doping, volatge decay, Li-ion batteries

Abstract

The practical applications of high-energy Li-rich layered oxides (LLOs) have been hindered by the severe performance degradation including voltage decay and capacity fading. The gradient construction toward high-activity interior and high-stability exterior, typically realized by gradually changed transition metal (TM) gradient in LLOs, can alleviate the performance degradation to certain degrees. Herein, a gradient design of Al/Mg dopants is demonstrated for the TM-gradient LLOs to further harmonize the high-activity interior and high-stability exterior, thereby forming the dual (TM and doping) gradients. As a result, a superior capacity retention of 86% and a minor voltage decay of 0.54 mV cycle^{-1} are achieved at 1 C after 300 cycles. The improved electrochemical stability of the dual-gradient LLO is attributed to the enhanced surface stability and suppressed bulk structure degeneration of LLOs upon electrochemical cycling. The dual-gradient design serves as an important approach to fabricate high-performance bulk LLOs toward applications.

Introduction

Li-ion batteries (LIBs) have been ubiquitous in today's electronic and energy applications, however, their further optimizations are strongly limited by the cathode materials with unsatisfying energy density.[1] Li-rich layered oxides (LLOs) are promising next-generation cathode materials for LIBs when considering their high energy densities (over 1000 Wh kg^{-1}).[2, 3] Unfortunately, severe voltage decay and poor cycling stability, which are induced by factors

including the structure degeneration, irreversible oxygen loss, interfacial side reactions, etc., are the primary issues latching the application of LLOs.[4-6] To overcome these shortcomings, various optimization methods such as element doping, surface coating, and cathode-electrolyte interphase modification have been applied.[7-10] However, new strategies focusing on the bulk design are highly required to intrincially optimize the structures and electrochemical performance of LLOs, which are also integrable with surface modification methods to realize application-level performance.

Recently, a transition metal (TM)-gradient design of bulk LLO (GLLO) with the high-activity core (Mn-rich) and high-stability surface (Mn-poor) was realized by fabricating gradually changed TM concentrations, which can noticeably optimize the comprehensive performance owing to the elegant differentiation control of TM concentration.[11, 12] It is worth noting that the gradient construction can improve the performance by mregulating the gradient slope of original TM elements without any external modifications. Therefore, the TM-gradient design can be integrated with other modification methods such as elemental doping to further improve the electrochemical performance of LLOs. In particular, the bulk elemental doping can be designed as graident distribution, which offers a new oppotunity to further harmonize the high-activity interior and high-stability exterior. Such a dual-gradient construction is of great merits to elegantly control bulk LLOs without complicated extra treatments, and thus of high value for practical applications.

Element doping has been widely reported as a simple and efficient method to stabilize the structures and improve the performance of LLOs.[13, 14] Up to now, various doing elements such as Al, Mg, Zr, Nb, and W have been employed to improve the electrochemical performance of LLOs.[7, 15-18] Among them, the light-weight and low-cost elements of Al is preferred for practical application, which can stablize LLOs by the the strong Al-O bonds.[19, 20] In addition, another low-cost element of Mg could insert into the Li layer due to its similar ionic radius of 0.072 nm with Li^+ (0.076 nm), which can stabalize the layered structure during cycling at high voltage.[21, 22] Compared with single element doping, the co-doping of multiple elements can combine the advantages of each dopant and better improve the electrochemical performance of LLOs.[23] In our recent study, a milder Al/Mg co-doped LLO present the advanced cycle performance via equilibrating the different characteristics of Al and Mg dopants.[24] Considering

the characteristics of Al and Mg dopants, it is anticipated that Al/Mg co-doping will play synergetic effects in optimizing gradient LLOs.

In this work, a dual-gradient construction including the TM gradient and the Al/Mg doping gradient is proposed for LLOs. The gradient doping is utilized to maintain the high activity in the core and enhance the stability of surface. Moreover, the Al dopant stabilizes the TM layer, while the Mg dopant maintains the layer spacing in the Li layer. As a result, the dual-gradient construction not only suppresses the structural transitions and side reactions at surface, but also reduces the volume change and oxygen vacancies of bulk material upon initial and long-term cycling, collectively leading to the superior electrochemical performance with alleviatived voltage decay and high capacity retention.

Results

Figure 1 shows the design strategy of gradient Al/Mg co-doped GLLO. According to our previous study, the electrochemical performance of GLLO is significantly enhanced by the composition gradient from high-activity core to high-stability surface, which is achieved by the appropriate TM gradient.[11] To further improve the electrochemical performance by enhancing the surface stability, the Al/Mg dopants, which can stabilize the layered structure, are introduced into GLLO by forming the gradient of gradually increased concentration from the center to the surface. In other words, the dual gradients are designed for GLLO including the TMs and Al/Mg dopants gradients.

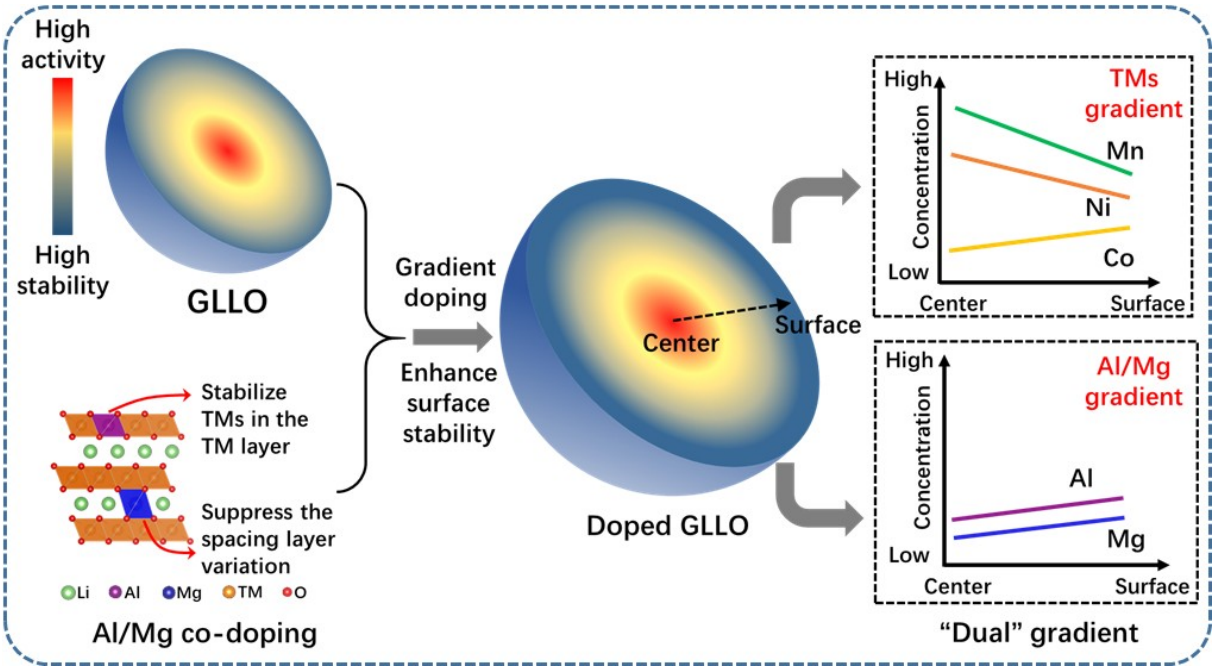

Figure 1. Schematic diagram of Al/Mg gradient co-doping of GLLO.

To prepare the gradient Al/Mg co-doped LLOs, the full-concentration gradient LLO (GLLO) was firstly synthesized by a co-precipitation method, and then the Al and Mg dopants were introduced by ALD coating followed by heating treatment. In each ALD cycle, Al and Mg precursors were co-introduced to deposit onto GLLO (Method Section). According to the ALD cycle numbers (1, 2, and 3), the doped GLLOs are denoted as GLLO-1AM, GLLO-2AM, and GLLO-3AM, respectively. The morphologies of the pristine GLLO and the three co-doped GLLOs were first examined by scanning electron microscope (SEM). **Figure 2**a shows that the typical co-doped GLLO-2AM maintains the secondary spherical aggregate (SSA) morphology of GLLO, and energy dispersive spectrum (EDS) maps demonstrate the uniform distributions of Mn, Ni, Co, Al and Mg elements at the GLLO-2AM surface. The SEM images and EDS results of other materials are shown in Figure S1 (supporting information, SI), which also present the SSA morphologies and uniform distributions of Mn, Ni, Co, Al, and Mg at the surface of particles. Representatively, Figure S2 presents a single SSA particle of GLLO-2AM, showing the regular sphere morphology with a particle size of ~10 μm. Moreover, the surface structure of the representative GLLO-2AM was investigated by high-resolution transmission electron microscopy (HRTEM). Compared with GLLO after ALD coating for 2 cycles but no heating treatment, which has uniform coating layer as shown in Figure 2b, GLLO-2AM obtained after

further heating treatment shows no coating layer (Figure 2c), indicating that Al and Mg were doped into the SSA particle.

To confirm the gradient co-doping of Al and Mg, the cross-section plane of a typical GLLO-2AM particle with a diameter of ~10 μm was prepared by focused ion beam (FIB) as shown in Figure 2d. Along the red arrow in the cross-section plane, the distributions of elements were evaluated by EDS line scanning. As shown in Figure 2e, Al and Mg demonstrate gradually increased contents from the center to the peripheral region, indicating their as-designed gradient distributions in GLLO-2AM. Meanwhile, Figure S3 shows that Mn, Ni, and Co also maintain the gradient distributions, suggesting the heating treatment after the ALD coating of GLLO does not erase the full concentration gradients of Mn, Ni, and Co in GLLO. Therefore, dual-gradient lithium-rich cathodes including TM (Mn, Ni, and Co) gradient and dopant (Al and Mg) gradient were successfully prepared.

The crystalline structures of all materials were examined by X-ray diffraction (XRD) as shown in Figure 2f. Most peaks in these patterns can be indexed with the layered $LiTMO_2$ structure ($R\bar{3}m$ space group), while a few peaks in the 2θ range of 20-24°can be indexed with the Li_2MnO_3 structure (C2/m space group), in agreement with the characteristic patterns of LLOs[25] The separations of the (006)/(102) and (108)/(110) diffraction peaks indicate that the highly ordered layered structures in GLLO were well maintained after the Al/Mg co-doping.[26] To obtain the composition ratios of $LiTMO_2$ and Li_2MnO_3 crystal domains, the Rietveld refinement based on two-phase model was carried out for all materials. For GLLO-2AM (Figure 2g), it can be seen that the experimental and calculation results are matched well, and the fractions of $LiTMO_2$ and Li_2MnO_3 are 62(3)% and 38(3)%, respectively. The Rietveld refinement results of other materials are presented in Figure S4, and the detailed data of Rietveld refinement are shown in Table S1. The fractions of $LiTMO_2$/Li_2MnO_3 in GLLO, GLLO-1AM, and GLLO-3AM are 60(2)/40(2)%, 58(3)/42(3)%, and 59(3)/41(3)%, respectively. Figure 2h outlines the fractions of $LiTMO_2$ and Li_2MnO_3 in the four materials. Obviously, the crystal domains of co-doped GLLOs are almost unchanged, indicating that Al/Mg gradient co-doping has negligible effect on the crystal domains of GLLOs.

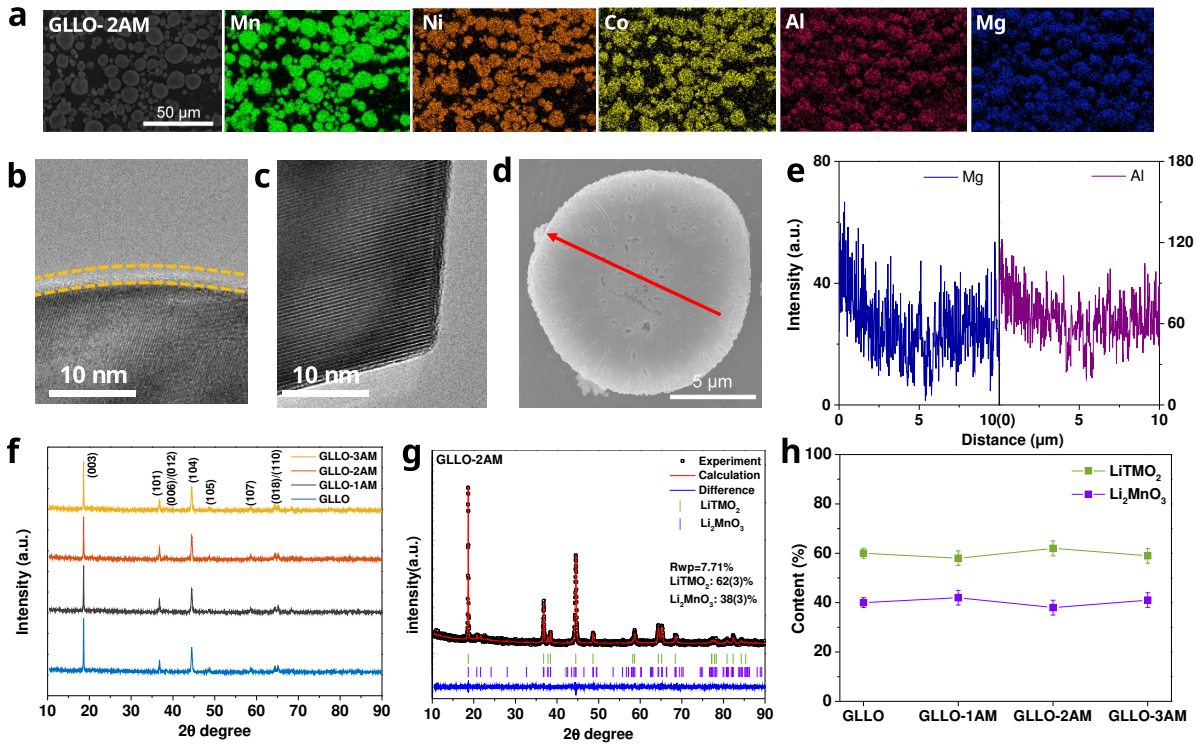

Figure 2. a) SEM image of GLLO-2AM and EDS maps of Mn, Ni, Co, Al, and Mg. b, c) Typical HRTEM image of GLLO after ALD coating for 2 cycles (b) and HRTEM image of GLLO-2AM with further heat treatment (c). d) SEM image showing the cross-section plane of GLLO-2AM. e) EDS line scans of Al and Mg dopants. f) XRD patterns of GLLO, GLLO-1AM, GLLO-2AM, and GLLO-3AM. g) Rietveld refinement results of GLLO-2AM based on two-phase model of $LiTMO_2$ and Li_2MnO_3. h) Fractions of $LiTMO_2$ and Li_2MnO_3 crystal domains in all materials according to the refinement results.

The electrochemical performance of the four materials was evaluated to investigate the effect of Al/Mg gradient co-doping on GLLO. **Figure 3**a shows the 1st-cycle charge-discharge curves, presenting the characteristic electrochemical profiles of LLOs including a typical two-stage charge curve for all materials. At a current density of 0.1 C (1 C = 200 mA g^{-1}) in the voltage range of 2-4.8 V, the charge/discharge capacities are 344/277, 334/267, 313/254, and 307/244 mAh g^{-1} for GLLO, GLLO-1AM, GLLO-2AM, and GLLO-3AM, respectively. Obviously, the charge profiles below 4.4 V, associated with the oxidation of transitional metal (Ni and Co) cations, almost overlap for all materials, which contribute an identical capacity of ~137 mAh g^{-1}. However, in the process of charging to 4.8 V, which is associated with oxygen anionic oxidation, the charge capacities decrease upon the increase of doping content (Table S2), indicating that the oxygen anionic activation is suppressed by the Al/Mg co-doping. Moreover, in the corresponding dQ/dV curves of the 1st-cycle charge-discharge profiles (Figure S5), all

materials display the similar peak at around 4.0 V in the charge process, but show a gradually weakened peak at around 4.5 V upon the increase of doping content, further indicating that the impervious Ni and Co activity and suppressed O activity are expressed in doped GLLOs.[27]

After activation at 25 °C, the cycle performance tested within 2-4.6 V at 1 C is shown in Figure 3b. At the beginning of cycling, GLLO exhibits a higher discharge capacity of 190 mAh g^{-1}, which decreases to 150 mAh g^{-1} after 300 cycles with a capacity retention of 80%. After Al/Mg gradient co-doping, the discharge capacities decrease from 188, 185, and 165 mAh g^{-1} to 154, 160, and 136 mAh g^{-1} after 300 cycles, corresponding to the capacity retentions of 82%, 86%, and 82% for GLLO-1AM, GLLO-2AM, and GLLO-3AM, respectively. Although the cycle performance can be improved after co-doping, GLLO-2AM exhibits the best cycle performance with the slight reduction of capacity, while GLLO-3AM with higher doping contents shows an apparent capacity reduction, suggesting the co-doping content should be elegantly controlled. In Figure 3c, the average voltage decays of the cathodes during 300 cycles are compared. It can be seen that the average voltage decay of GLLO decreases from 3.61 to 3.41 V, corresponding to a decay rate of about 0.67 mV $cycle^{-1}$. For GLLO-1AM, GLLO-2AM, and GLLO-3AM, the average voltage decay rates are 0.6, 0.54, and 0.7 mV $cycle^{-1}$. Therefore, the electrochemical stability of GLLO-2AM is compared with other representative modified LLOs,[7, 10, 15, 17, 18, 23, 28-33] as shown in Figure 3d. Obviously, GLLO-2AM in this work presents a minimum voltage decay of 0.54 mV $cycle^{-1}$ at 1 C for 300 cycles, suggesting the superiority of GLLO-2AM among various LLOs. Combining with the high capacity retention of GLLO-2AM, the Al/Mg gradient co-doping can be considered as a potential modification strategy for practical application.

The rate performance of GLLO and GLLO-2AM was further examined at 0.1, 0.2, 0.5, 1, 2, and 5 C (Figure S6a). It can be seen that although the capacities of GLLO are higher than those of GLLO-2AM, the capacity reductions of both materials upon the increase of rate are similar. For example, when the rate is increased from 0.1 C to 5 C, both materials show a similar capacity reduction of ~150 mAh g^{-1}, indicating that the rate performance was not significantly influenced by the Al/Mg co-doping. Furthermore, the Li^+ diffusion coefficient (D_{Li+}) was calculated through the GITT test (Figure S6b-d). The similar D_{Li+} values of GLLO and GLLO-2AM indicate that Al/Mg gradient co-doping have minor effect on the Li^+ migration kinetics.

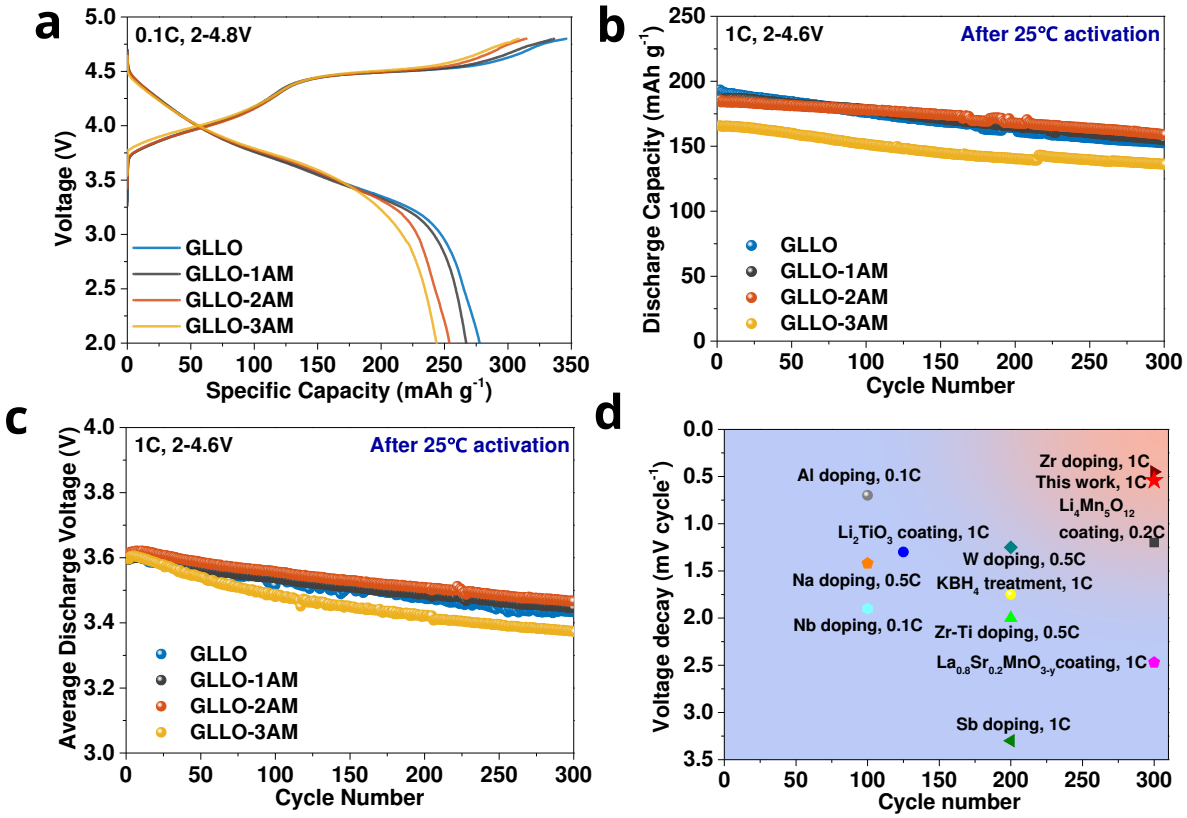

Figure 3. a) Initial charge-discharge curves of GLLO, GLLO-1AM, GLLO-2AM, and GLLO-3AM within 2-4.8 V at 0.1 C (1 C = 200 mA g^{-1}) at 25 °C. b, c) Cycle performance (b) and average discharge voltages (c) within 2-4.6 V at 1 C and 25 °C after the activation at 25 °C. d) Comparisons of voltage decay in this work with those from representative modification reports for LLOs.

The concentrations of Al and Mg at the exterior of GLLO-2AM are the highest, which may noticeably influence the surface structures and electrochemical reactions. Therefore, the influence of dopants on the stabilities of surface structures was investigated. **Figure 4**a, b show the Raman spectra of cathode materials at different states. Before cycling, GLLO and GLLO-2AM exhibit similar typical Raman spectra of LLOs, including the E_g peak (492 cm^{-1}) with O-TM-O bending mode and the A_{1g} peak (598 cm^{-1}) with the M-O stretching mode (Figure 4a).[34, 35] After 300 cycles, the E_g peak and A_{1g} peak can still be clearly seen in the Raman spectrum of GLLO-2AM, indicating that the layered structure maintains on the surface region. In contrast, the two peaks in the cycled GLLO are almost invisible, suggesting the severe structure reconstruction upon cycling. In addition, a new shoulder peak located at 640 cm^{-1} (green dashed line) appears for both materials, which is well matched with the spinel structure.[15, 36] However,

this peak is much stronger in GLLO than that in GLLO-2AM, implying the structure degradation at the surface is suppressed by the Al/Mg co-doping.

The surface spinel structure was further probed by high angle annular dark field scanning transmission electron microscopy (HAADF-STEM), and the results are shown in Figure 4c, d. Figure 4c shows the HAADF-STEM image of GLLO after 300 cycles. It can be observed that the surface structure within 5 nm thickness is different from the inner structure, as separated by the yellow dashed line. In order to identify the surface spinel structure, the region A on the surface in Figure 4c was converted by fast Fourier transform (FFT) as shown in Figure 4d. Consequently, the FFT pattern can be well matched to the spinel structure along the $[0\bar{1}1]$ direction. Meanwhile, Figure 4e displays the magnified HAADF-STEM image of region A, which can also be indexed to the atomic arrangement of the spinel structure. In contrast, according to the FFT pattern (Figure 4g) and atomic arrangement (Figure 4h), GLLO-2AM exhibits a spinel structure layer with a thickness of only 2 nm (Figure 4f), indicating the deteriorative structure transformation on the surface is suppressed. Based on the Raman and STEM studies, the gradient distribution of Al/Mg can lead to the improved stability of surface structures from the perspectives of average and local structures.

Furthermore, the surface chemical states of GLLO and GLLO-2AM after 300 cycles were investigated. Figure 4i, j displays the Mn 2p XPS spectra of cycled GLLO and GLLO-2AM. The Mn 2p spectra of cycled GLLO can be divided into two components of Mn^{4+}/Mn^{3+} with a ratio of 52.7/43.3%, while the ratio of Mn^{4+}/Mn^{3+} in the cycled GLLO-2AM is 66.7/33.3%. Obviously, GLLO-2AM has less Mn^{3+} (33.3%) than that of GLLO (43.3%). When more low-valence states of Mn are activated, an intensified voltage decay and the appearance of more spinel structures would occur,[5] which coincides to the Raman and STEM results of GLLO. Therefore, the gradient co-doping of Al/Mg improves the maintenance of high Mn valence states. Figure S7 shows the C 1s XPS spectra of GLLO and GLLO-AM after 300 cycles. In general, the C=O peak is contributed from Li_2CO_3 produced by the surface side reactions and electrolyte decomposition.[23, 37] Apparently, the weaker C=O peak in GLLO-2AM indicates the surface side reactions related to electrolyte decomposition are suppressed after Al/Mg gradient co-doping. Moreover, the F1s XPS spectra of GLLO and GLLO-AM after 300 cycles are shown in Figure S8, which are contributed by the formation of LiF and $Li_xPO_yF_z$ that generated from the complex surface reaction between electrode and electrolytes.[8] The weaker peaks in GLLO-

2AM suggests that the surface chemical stability is improved by the Al/Mg gradient co-doping. Combining the Raman, STEM, and XPS results, the Al/Mg gradient co-doping significantly improves the surface structural and chemical stabilities, which is helpful to improve the electrochemical stability.

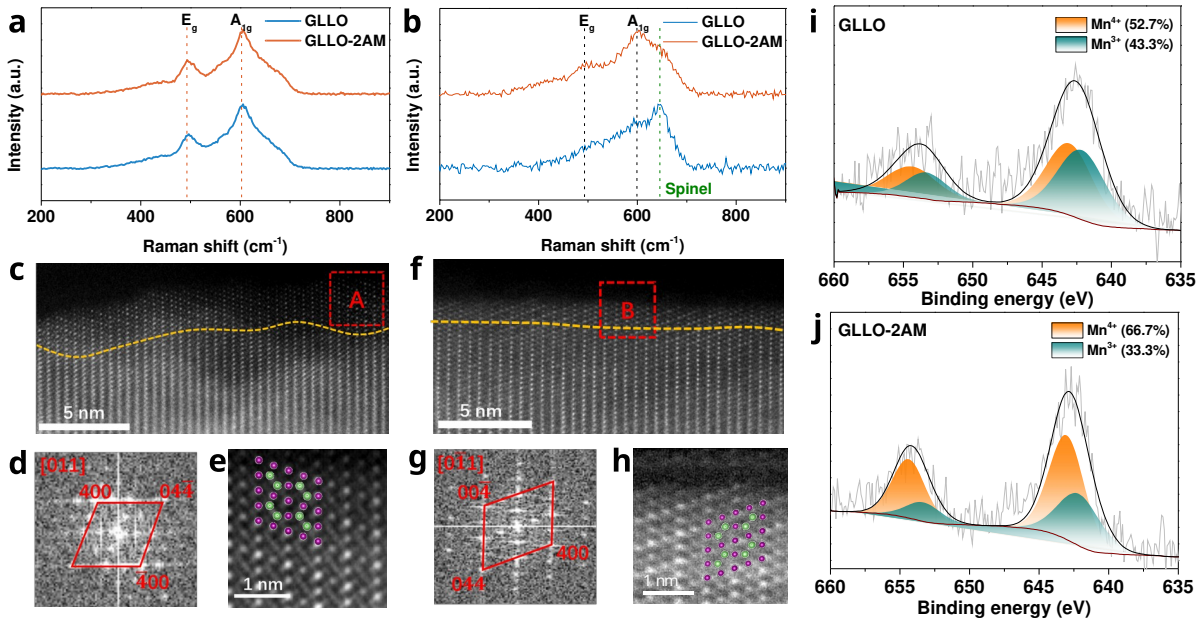

Figure 4. a, b) Raman spectra of GLLO and GLLO-2AM in the pristine state (a) and after 300 cycles (b). c-e) HAADF-STEM image of GLLO after 300 cycles (c), corresponding FFT patterns (d) and enlarged HAADF-STEM images (e) of region A in (c). f-h) HAADF-STEM image of GLLO-2AM after 300 cycles (f), corresponding FFT patterns (g) and enlarged HAADF-STEM images (h) of region B (f). Purple and green balls represent the TM and Li atoms, respectively. i, j) Mn 2p XPS spectra of GLLO (i) and GLLO-2AM (j) after 300 cycles.

The effects of Al/Mg co-doping on the cathode materials in the initial several cycles were further studied through *in situ* and *ex situ* tests. *In situ* XRD was carried out to investigate the overall structure stability of GLLO and GLLO-2AM during electrochemical cycling. Figure S9 shows the 2D contour plots of XRD patterns and the corresponding time-voltage curves for GLLO and GLLO-2AM during the initial two electrochemical cycles. For a clearer comparison of the structural evolution and stability of GLLO and GLLO-2AM, Figure 5a, b shows the variations of the (003) peak, lattice parameters *a*, *c*, and cell volume *V*. It can be found that the (003) diffraction peaks of GLLO and GLLO-2AM exhibit a similar shift with the progress of charge and discharge. During the charge process below 4.4 V, the (003) peaks shift to lower 2θ degree, which is attributed to the expanded interlayer spacing caused by the increased

electrostatic repulsion in neighboring oxygen slabs upon Li^+ extraction from Li layer. In the charge plateau region (~4.5 V), the (003) peaks maintain at around 18.4°, which corresponds to the Li_2MnO_3 activation with the Li^+ extraction from the $LiMn_2$ layer.[38] At the end of charge to 4.8 V, the (003) peaks shift to higher 2θ degree, which is associated with the shrinkage of interlayer spacing caused by the formation of "Li-Mn dumbbell" structure.[29] During the discharge process, the (003) peaks show reversible variation corresponding to the Li^+ insertion process. In the subsequent cycle, the similar variation of (003) peak can be observed due to the similar delithiation-lithiation mechanism. Differently, the (003) peak of GLLO shifts by ~0.44° at the end of charge to 4.8 V, while that of GLLO-2AM shows less shift of ~0.38°, indicating that the interlayer structure of GLLO-2AM is more stable. Considering that the ionic radius of Mg^{2+} (0.72 Å) is close to that of Li^+ (0.76 Å), it should be easier for Mg^{2+} to occupy the Li site in Li layer. Moreover, our study showed that nearly half doping amount of Mg^{2+} (44%) would like to occupy the Li site in Li layer, while a little Al^{3+} (7%) of doping amount occupy the Li site in Li layer, indicating that Mg is more easily to dope into the Li layer. For layered cathode materials, Mg^{2+} doped in Li layer can play an important role in suppressing the layer spacing varitation.[24] The less shift of (003) peak in GLLO-2AM indicates that Mg might be doped into the Li layer, thus stabilizing the interlayer structure of GLLO.[22]

In addition, for the lattice parameter *a*, the variation is affected by the redox of TM ions. When the TM ions are oxidized during the charge process till 4.4 V, the TM-O bonds are shortened due to the decrease of ionic radius of TM ions, resulting in the reduction of lattice parameter *a*. During further charge to 4.8 V, the lattice parameter *a* remains constant since the charge compensation is governed by the activated oxygen anions. During the discharge process, lattice parameter *a* gradually increases with the reduction of TM ions. It can be seen that the Δ*a* values of GLLO (0.05 Å) and GLLO-2AM (0.04 Å) are similar, which is because of the similar content of TMs. The lattice parameter *c* mainly reflects the change of Li layer spacing along the *c*-axis, therefore the increasing/decreasing lattice parameter *c* represents the expanded/shrunken layer spacing. GLLO-2AM exhibits smaller Δ*c* (0.21 Å) than GLLO (0.26 Å), further indicating that the interlayer structure is more stable after Al/Mg co-doping. Moreover, the variations of cell volume (Δ*V*) show a considerable decrease of Δ*V* from 3.7 $Å^3$ in GLLO to 2.7 $Å^3$ in GLLO-2AM. In general, the larger Δ*V* during charge-discharge process will degenerate the structural stability, thus causing the decay of electrochemical performance.[39] Therefore, the Al/Mg

gradient co-doping improves the overall structure stability, which is beneficial to the electrochemical performance of GLLO.

The *in situ* DEMS was used to characterize the effect of Al/Mg gradient co-doping on the gas release. As shown in Figure 5c, d, neither GLLO nor GLLO-2AM show the O_2 generation in the 1st cycle, suggesting that the irreversible O_2 release is not severe for both materials. On the other hand, CO_2 signals could be detected, whereas GLLO-2AM exhibits less CO_2 release in the high voltage region of 4.5-4.8 V than that of GLLO. It has been reported that CO_2 is originated from interfacial side reactions of LLOs at high voltage and decomposition of electrolyte.[40, 41] Since the same electrolyte (1 M $LiPF_6$ dissolved in EC/DEC) was used for the *in situ* batteries, it is reasonable that the weakened release of CO_2 in GLLO-2AM originates from the suppression of surface side reactions, which could be attributed to the improved surface structural and chemical stabilities.

Moreover, the thermal stabilities of GLLO and GLLO-2AM were further investigated by differential scanning calorimetry (DSC) based on the *ex situ* samples at charge state. Figure 5e presents the DSC curves of these two samples at the charge cut-off voltage of 4.4 V. Obviously, a broad exothermic peak nearly 300 ℃ is observed both in two samples. However, GLLO-2AM shows the exothermic peak at higher temperature of 308 ℃ than that of 292 ℃ in GLLO, and possesses less thermal release of 122 J g^{-1} than that of 136 J g^{-1}. In addition, the DSC curves at higher charge cut-off voltage of 4.8 V are shonw in Figure 5f. It can be seen that a weak peak appears below 200 ℃ in each sample, indicating the thermal stability is weakened slightly when the samples are charged to higher voltage. Even so, the temperature of the two exothermic peaks in GLLO-2AM (199/298 ℃) is still higher than that in GLLO (178/267 ℃). Moreover, the exothermic peak of GLLO-2AM also shows lower total thermal release of 313 J g^{-1}, compared with that of 372 J g^{-1} in GLLO. Therefore, GLLO-2AM exhibits exothermic peaks at higher temperature and possesses less thermal release both at 4.4 and 4.8 V, indicating the Al/Mg gradient co-doping is beneficial to improve the thermal stability and battery safety.

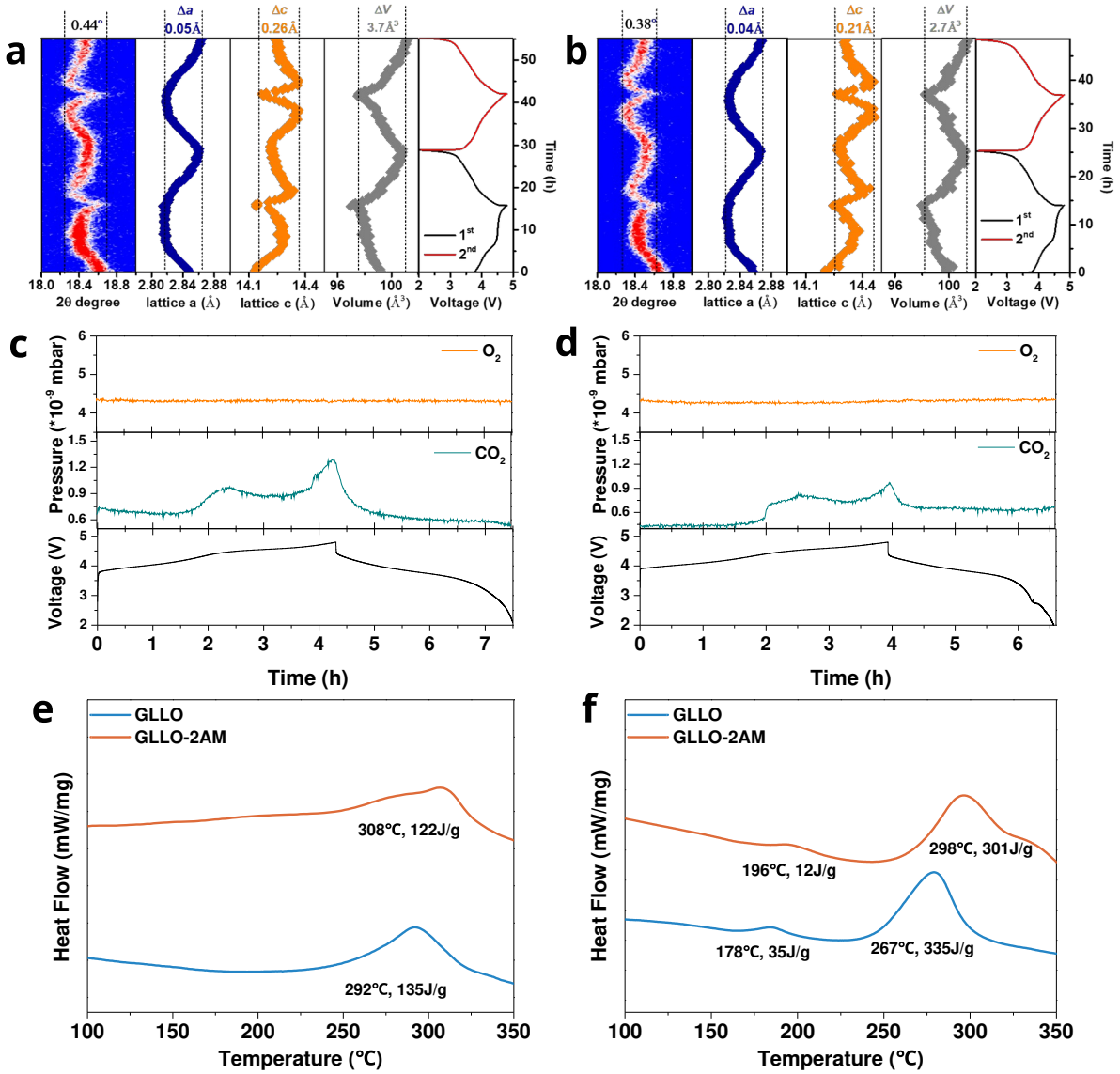

Figure 5. a, b) The variations of (003) peaks in the contour plot of *in situ* XRD patterns between 18°-19°, lattice parameters *a, c*, cell volume *V*, and corresponding time-voltage curves for GLLO (a) and GLLO-2AM (b). c, d) O_2 and CO_2 release profiles during the initial charge-discharge cycle obtained by *in situ* DEMS for GLLO (c) and GLLO-2AM (d). e, f) DSC curves of GLLO and GLLO-2AM at different charge cut-off voltage of 4.4 (e) and 4.8V (f).

To further investigate the structure stability in long-term cycles, the GLLO and GLLO-2AM electrodes after 300 cycles were characterized. **Figure 6**a shows the XRD patterns of cycled GLLO and GLLO-2AM. Noticeably, the separation of (006)/(102) peaks still maintain in the cycled GLLO-2AM, but disappears in the cycled GLLO, indicating that the layered structure is stabilized after Al/Mg gradient co-doping. Moreover, the Rietveld refinement based on the two-phase mode of layered and spinel structures was carried out to obtain the contents of spinel

structures and oxygen vacancies in the cycled cathodes. Figure S10 and Figure 6b show the Rietveld refinement results of cycled GLLO and GLLO-2AM. The experiment data match well with the calculation fitting curves. The contents of spinel structures and oxygen vacancies are shown in Figure 6c. Obviously, the cycled GLLO-2AM shows less spinel structure of 2.2(5)% than that of cycled GLLO-AM (8.1(2)%), which further indicates that Al/Mg gradient co-doping could inhibit the structure reconstruction. In addition, the oxygen vacancies generated in cycled GLLO and GLLO-2AM are 18.2(2)% and 10.1(4)%, respectively, indicating that the formation of oxygen vacancies is suppressed by the Al/Mg gradient co-doping.

With the stabilized surface and less oxygen vacancies, GLLO-2AM electrodes demonstrate relatively high energy density (Figure 3). In order to confirm the existence and persistence of lattice oxygen redox in the electrochemical cycle process, high-efficiency mapping of resonant inelastic X-ray scattering (mRIXS) was performed on the samples with different representative states, which has been established as a reliable probe for characterizing the oxygen redox behavior. mRIXS identifies oxidized lattice oxygen through two fingerprinting features at the excitation energy 531 eV: a dominant feature at around 523.7 eV emission energy and a energy loss feature close to the elastic line.[42-44] Figure 6e-g display the O *K*-edge mRIXS images of a series of GLLO-2AM electrodes at different charge/discharge states indicated on the cycling curve in Figure S11. Both of the dominant feature at 523.7 eV emission energy highlighted as red circle and the energy loss feature near the elastic peak indicated as white arrow appear at fully charged state in Figure 6e-g, and disappear at the pristine state in Figure 6d and the fully discharged state in Figure 6f-h. This direct comparison clearly indicates oxygen redox reaction is involved in whole electrochemical cycling process, at least over 300 cycles as expected. More strikingly, the intensity of 523.7 eV features (red circles) are almost same for first charged state in Figure 6e and for 300th charged state in Figure 6g, which indicates the perfect reversibility and retention of the lattice oxygen redox upon 300 cycles.[45] Comparing with the traditional Li-rich materials,[46] dual-gradient doping provide better cyclability of the lattice oxygen redox upon cycling. Therefore, although the surface degradation and oxygen vacancies are mitigated through the dual-gradient doping, the reversible lattice oxygen redox reaction is maintained to offer the high-energy operation.

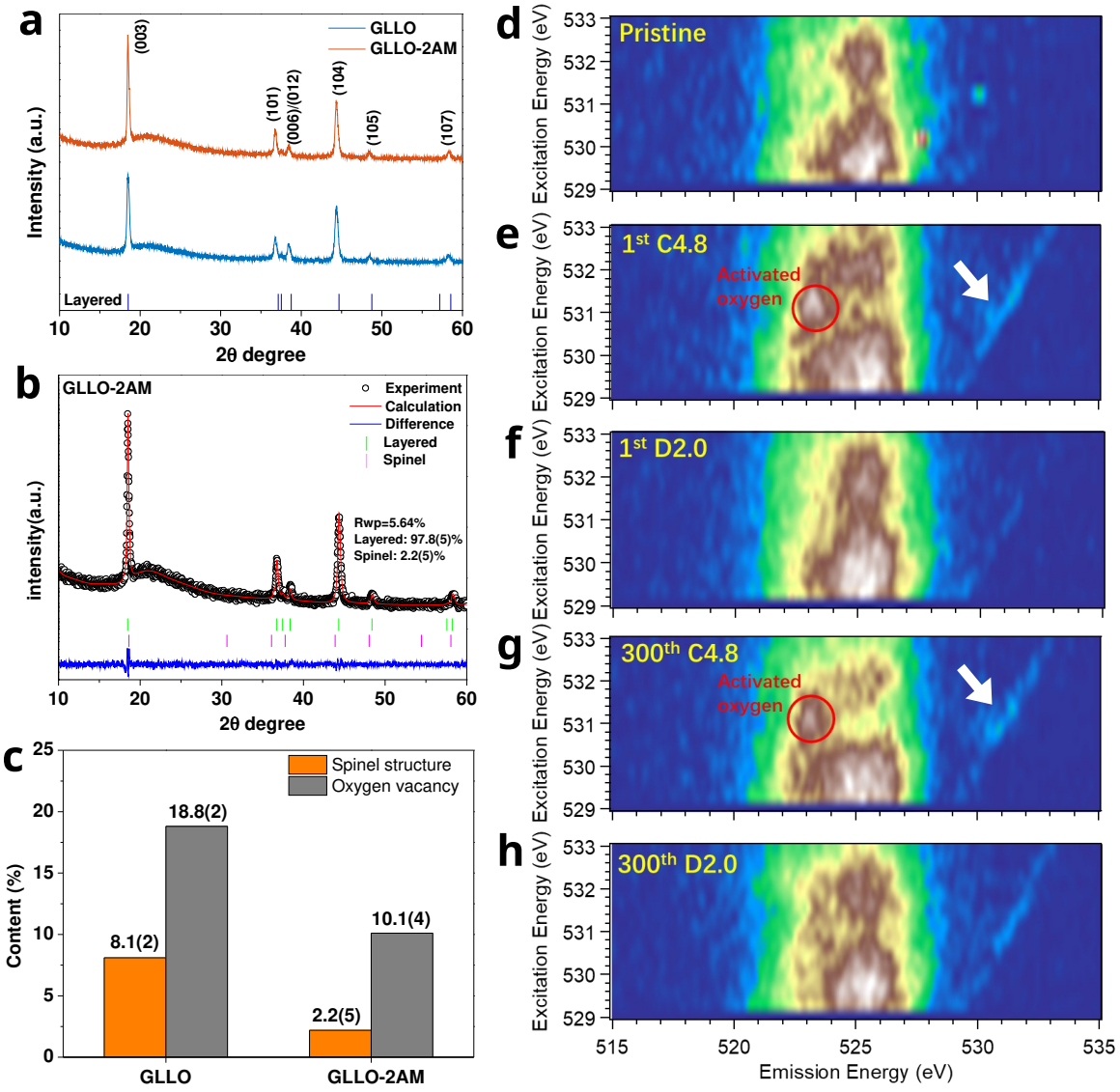

Figure 6. a) XRD patterns of GLLO and GLLO-2AM after 300 cycles. b). Rietveld refinement results of GLLO-2AM after 300 cycles based on two-phase model of layered and spinel. c) The contents of spinel structure and oxygen vacancy obtained by the Rietveld refinement of XRD patterns. d-h) O K-edge mRIXS collected on GLLO-2AM with different states, (d) pristine, (e) the first cycle fully charged state marked as 1 C4.8, (f) the first cycle fully discharged state marked as 1st D2.0, (g) the 300th cycle fully charged state marked as 300th C4.8, and (h) the 300th cycle fully discharged state marked as 300th D2.0. The electrochemical profile of all representative states (d-h) are shown in Figure S11.

According to the above characterization studies, Al and Mg are verified to co-dope into GLLO with a gradient distribution, and the electrochemical performance of GLLO can be improved by the Al/Mg gradient co-doping, which is attributed to the enhanced structure and chemical stabilities. It is worth noting that the gradient co-doping is employed in our study instead of uniform co-doping, because the gradient co-doping can harmonize with the original TMs

concentration gradient in GLLO, thereby further stabilize the material upon electrochemical cycling. In GLLO, the TM gradient is designed to fabricate the high active center and high stable surface in a particle. If the doped Al and Mg are uniformly distributed or have high contents in the particle center, they will inevitably affect or even degradate the highly active center in GLLO, resulting in a substantial capacity decrease. On the contrary, when a gradient doping with a high-content surface and low-content center is realized, not only the influence of doping elements on the high active center is reduced, but also the surface stability of GLLO is enhanced. In fact, we have demonstrated the Al and Mg have different characterization according to their doping site in uniform LLOs, and launched a milder Al/Mg co-doping LLO with enhanced cycle performance. In this study, the electrochemical performance and characterization results also prove that the gradient doping of Al and Mg is suitable for our gradient Li-rich cathode material. Furthermore, the dual gradient design in GLLO-2AM not only suggests that the integration of multiple gradients may express synergistic effects with proper design, but also shows that there is still a lot of space in bulk doping design..

Conclusion

In summary, to fabricate LLOs with active interior and stable exterior, a dual-gradient design has been proposed by combining the TM gradient composition and Al/Mg gradient doping. The gradually increased contents of Al/Mg dopants from the core to the surface of secondary particles further stabilize the TM-gradient LLOs while maintaining the high activity, thereby improving the electrochemical performance of dual-gradient LLOs. As a result, the optimal dual-gradient GLLO-2AM exhibits the highest capacity retention of 86% and lowest average voltage decay of 0.54 mV $cycle^{-1}$ at 1 C within 300 cyels after the activation at 25 ℃. Surface-sensitive characterizations have shown that after the dual gradient design, the layer-to-spinel transition can be restrained, and the chemical valance states of Mn can be increased to attenuate the Jahn-Teller effect. Furthermore, *in situ* XRD and *in situ* DEMS demonstrate that the volume variation and gas release of GLLO-2AM can be suppessed in the initial cycles, respectively. Such a structure stabilization effect was found to be maintained even 300 cycles, with largely reduced spinel structures and oxygen vacancies as verified by the XRD Rietveld refinement results. This work offers a new strategy to optimize both the surface and bulk properties of LLOs and other oxide cathode materials toards high-energy batteries.

Experimental Section

Synthesis of GLLO: The concentration gradient LLO (GLLO) was synthesized by sintering carbonate precursors and appropriate lithium carbonate (5% Li excess) under 600 °C for 5 h and then 900 °C for 12 h. The carbonate precursors were obtain by the co-precipitation method as reported in our previous work.[11]

Synthesis of GLLO-AM: To obtain the Al/Mg co-doped GLLO (GLLO-AM), the Al/Mg oxides coating layer was firstly fabricated by the atomic layer deposition (ALD, Anstrom) technique on GLLO. During the coating process, the reaction temperature was maintained at 150 °C, and the precursor sources of Al and Mg were trimethylaluminum ($(CH_3)_3Al$) and Bis(cyclopentadienyl) magnesium ($Mg(C_5H_5)_2$), respectively. Firstly, through the twice pulse process of $(CH_3)_3Al$ and H_2O and once pulse process of $Mg(C_5H_5)_2$ and H_2O, the Al/Mg oxides layer was coated on the surface of GLLO. Then, the above deposition processes were carried out for 1, 2, and 3 cycles, respectively. In detail, the pulse/reaction times of $(CH_3)_3Al$, $Mg(C_5H_5)_2$, and H_2O were 0.3 s/60 s, 0.2 s/120 s, and 0.6 s/60 s, respectively, where H_2O was used for cleaning. Subsequently, the GLLOs treated by ALD for 1, 2 and 3 cycles were heated at 400 °C for 5h, and cooled in the furnace to obtain the final products, denoted as GLLO-1AM, GLLO-2AM, and GLLO-3AM, respectively.

Characterization: The morphologies of GLLO and GLLO-AM were investigated by SEM (Hitachi SU8020), and the element distributions in FIB treated equatorial plane were determined by energy EDS line scanning. XRD patterns were obtained using X-ray diffractometer (Bruker D8 ADVANCE) with Cu Kα radiation (λ = 1.5405 Å) to examined the structure information, and the *in situ* XRD was collected to obtain the cell parameters during the initial two electrochemical cycles. TOPAS5 software was used to refined all the XRD patterns. In addition, the *in situ* DEMS (Hiden Analytical, HPR-20) was carried out to evaluate the O_2 and CO_2 generations in the initial cycle. The mRIXS results were collected at Beamline 8.0.1 of the Advanced Light Source of the Lawrence Berkeley National Laboratory (LBNL). All the samples for RIXS experiments were prepared and processed in Ar-filled glove box to avoid any air or humidity exposure. For the surface information, the elemental valences were measured by XPS (Thermo Scientific Escalab, 250Xi), and the surface structures were detected by Raman spectrum (WITec, alpha300) and HAADF-STEM (JEOL JEM-ARM200CF STEM). The thermal stabilities of GLLO and GLLO-AM were evaluated by DSC (NETZSCH, STA-

449F3) test after they were charged at 4.4 and 4.8 V in coin cells. The average chemical compositions of GLLO-were was measured by inductively coupled plasma (ICP) spectroscopy (OPTIMA7000DV).

Electrochemical Measurements: To prepare the electrodes, the active material (GLLO or GLLO-AM), carbon black, and polytetrafluoroethylene (PVDF) binder were mixed at a weight ratio of 8:1:1 and dispersed in Nmethyl-2-pyrrolidone (NMP) solvent to form the slurries. Subsequently, the mixed slurries were coated on Al foil current collectors using the scraper, and then dried at 120 °C overnight in a vacuum oven. Finally, the electrodes were obtained after stamping the dried slurries into circular sheets with 12 mm diameter. The loading active material was around 3.5 mg cm^{-2}. The CR2032-type coin cells were assembled with the above electrodes, Celgard 2400 separator, Li foil, and electrolyte (bought from GUOTAI-HUARONG company) in an Ar-filled glove box (H_2O and O_2 contents were below 0.1 ppm). The batteries were activated in the first cycle at 25 ℃ between 2.0–4.8 V (vs Li^+/Li) with a current density of 0.1 C (1 C = 200 mA g^{-1}) and cycled in 300 cycles between 2.0–4.6 V at 1 C. The rate performances were tested at 0.1, 0.2, 0.5, 1, 2, and 5 C between 2.0-4.6 V after the activation at 25 ℃. The galvanostatic intermittent titration (GITT) was carried out at 0.1 C in the voltage range of 2.0-4.8 V. For the *in situ* XRD and *in situ* DEMS studies, the *in situ* batteries were test at 0.1C within 2-4.8 V. All the electrochemical performances were measured on the LAND CT2001C battery test system, while the batteries used for *in situ* DEMS were test on a Chenhua (CHI660E) electrochemical workstation.

Acknowledgements

This work was financially supported by National Key R&D Program of China (2022YFB2404400), National Natural Science Foundation of China (92263206 and 21975006),, and Beijing Natural Science Foundation (2222001 and KM202110005009). Soft X-ray spectroscopy were performed at the BL 8.0.1.1 (iRIXS) endstation at the Advanced Light Source (ALS), a USA DOE Office of Science User Facility at Lawrence Berkeley National Laboratory (LBNL), under DOE contract no. DE-AC02-05CH11231.

Received: ((will be filled in by the editorial staff))
Revised: ((will be filled in by the editorial staff))
Published online: ((will be filled in by the editorial staff))

ToC Figure ((Please choose one size: 55 mm broad × 50 mm high **or** 110 mm broad × 20 mm high. Please do not use any other dimensions))

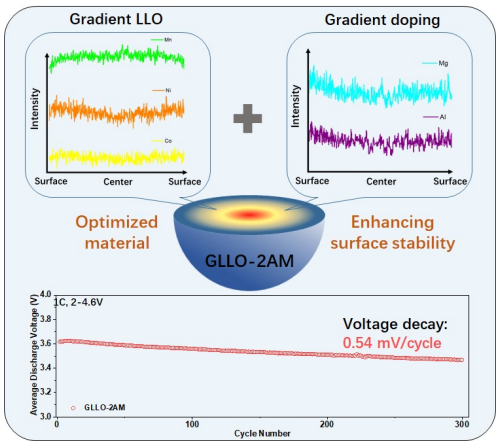

[1] V. Etacheri, R. Marom, R. Elazari, G. Salitra, D. Aurbach, *Energy & Environmental Science* **2011**, *4*, 3243.
[2] S. Cui, M. Gao, G. Li, X. Gao, *Adv. Energy Mater.* **2021**, *12*, 2003885.
[3] X. Zhang, B. Wang, S. Zhao, H. Li, H. Yu, *eTransportation* **2021**, *8*, 100118.
[4] D. Mohanty, J. Li, D. P. Abraham, A. Huq, E. A. Payzant, D. L. Wood, C. Daniel, *Chem. Mater.* **2014**, *26*, 6272.
[5] E. Hu, X. Yu, R. Lin, X. Bi, J. Lu, S. Bak, K.-W. Nam, H. L. Xin, C. Jaye, D. A. Fischer, K. Amine, X.-Q. Yang, *Nature Energy* **2018**, *3*, 690.
[6] J. Zhao, X. Zhang, Y. Liang, Z. Han, S. Liu, W. Chu, H. Yu, *ACS Energy Letters* **2021**, *6*, 2552.
[7] J. Meng, L. Xu, Q. Ma, M. Yang, Y. Fang, G. Wan, R. Li, J. Yuan, X. Zhang, H. Yu, L. Liu, T. Liu, *Adv. Funct. Mater.* **2022**, 2113013.
[8] E. Wang, Y. Zhao, D. Xiao, X. Zhang, T. Wu, B. Wang, M. Zubair, Y. Li, X. Sun, H. Yu, *Adv. Mater.* **2020**, *32*, e1906070.
[9] W. Guo, C. Zhang, Y. Zhang, L. Lin, W. He, Q. Xie, B. Sa, L. Wang, D. L. Peng, *Adv. Mater.* **2021**, *33*, e2103173.
[10] J. Liu, Z. Wu, M. Yu, H. Hu, Y. Zhang, K. Zhang, Z. Du, F. Cheng, J. Chen, *Small* **2022**, e2106337.
[11] T. Wu, X. Liu, X. Zhang, Y. Lu, B. Wang, Q. Deng, Y. Yang, E. Wang, Z. Lyu, Y. Li, Y. Wang, Y. Lyu, C. He, Y. Ren, G. Xu, X. Sun, K. Amine, H. Yu, *Adv. Mater.* **2021**, *33*, e2001358.
[12] L. W. Haotian Yang, Yuqiang, Zengqing Zhuo, Tianhao Wu, Jie Liu, Ligang Xu, Haozhe Du, Shiqi Liu, Lingqiao Wu, Shu Zhao, Mingxue Tang, Wanli Yang, Haijun Yu, *PNAS* **2024**.
[13] P. K. Nayak, E. M. Erickson, F. Schipper, T. R. Penki, N. Munichandraiah, P. Adelhelm, H. Sclar, F. Amalraj, B. Markovsky, D. Aurbach, *Advanced Energy Materials* **2018**, *8*, 1702397.
[14] J. Zheng, S. Myeong, W. Cho, P. Yan, J. Xiao, C. Wang, J. Cho, J. G. Zhang, *Advanced Energy Materials* **2016**, *7*, 1601284.
[15] P. K. Nayak, J. Grinblat, M. Levi, E. Levi, S. Kim, J. W. Choi, D. Aurbach, *Advanced Energy Materials* **2016**, *6*, 1502398.
[16] R. Yu, X. Wang, Y. Fu, L. Wang, S. Cai, M. Liu, B. Lu, G. Wang, D. Wang, Q. Ren, X. Yang, *Journal of Materials Chemistry A* **2016**, *4*, 4941.
[17] J. Zhang, Q. Zhang, D. Wong, N. Zhang, G. Ren, L. Gu, C. Schulz, L. He, Y. Yu, X. Liu, *Nature Communications* **2021**, *12*, 3071.
[18] S. Liu, Z. Liu, X. Shen, W. Li, Y. Gao, M. N. Banis, M. Li, K. Chen, L. Zhu, R. Yu, Z. Wang, X. Sun, G. Lu, Q. Kong, X. Bai, L. Chen, *Advanced Energy Materials* **2018**, *8*, 1802105.
[19] M. Ha, A. Hajibabaei, D. Y. Kim, A. N. Singh, J. Yun, C. W. Myung, K. S. Kim, *Advanced Energy Materials* **2022**, 2201497.
[20] H. Zhang, H. Liu, L. F. J. Piper, M. S. Whittingham, G. Zhou, *Chem. Rev.* **2022**.
[21] C. Pouillerie, L. Croguennec, Ph. Biensan, P. Willmann, C. Delmas, *J. Electrochem. Soc.* **2000**, *147*, 2061.

[22] Y. Huang, Y. Zhu, H. Fu, M. Ou, C. Hu, S. Yu, Z. Hu, C. Chen, G. Jiang, H. Gu, H. Lin, W. Luo, Y. Huang, *Angew. Chem. Int. Ed.* **2021**, *60*, 4682.
[23] E. Wang, D. Xiao, T. Wu, X. Liu, Y. Zhou, B. Wang, T. Lin, X. Zhang, H. Yu, *Adv. Funct. Mater.* **2022**, 2201744.
[24] X. Z. T. Wu, Y. Li, H. Du, T. Liu, Y. Yang, Z. Zhang, X. Liu, Q. Huang, Y. Ren, J. Qu, S. Zhao, B. Wang, R. Zheng, K. Amine, H. Yu, *Adv. Mater.* **2024**.
[25] H. Yu, H. Kim, Y. Wang, P. He, D. Asakura, Y. Nakamura, H. Zhou, *Phys. Chem. Chem. Phys.* **2012**, *14*, 6584.
[26] J. Wang, B. Qiu, H. Cao, Y. Xia, Z. Liu, *J. Power Sources* **2012**, *218*, 128.
[27] G. Assat, D. Foix, C. Delacourt, A. Iadecola, R. Dedryvere, J. M. Tarascon, *Nat Commun* **2017**, *8*, 2219.
[28] Q. Ma, Z. Chen, S. Zhong, J. Meng, F. Lai, Z. Li, C. Cheng, L. Zhang, T. Liu, *Nano Energy* **2021**, *81*, 105622.
[29] X. D. Zhang, J. L. Shi, J. Y. Liang, Y. X. Yin, J. N. Zhang, X. Q. Yu, Y. G. Guo, *Adv. Mater.* **2018**, *30*, e1801751.
[30] C. Yan, Q. Shao, Z. Yao, M. Gao, C. Zhang, G. Chen, Q. Sun, W. Sun, Y. Liu, M. Gao, H. Pan, *Small* **2022**, 2107910.
[31] Z. Feng, H. Song, Y. Li, Y. Lyu, D. Xiao, B. Guo, *ACS applied materials & interfaces* **2022**, *14*, 5308.
[32] S. Hu, Y. Li, Y. Chen, J. Peng, T. Zhou, W. K. Pang, C. Didier, V. K. Peterson, H. Wang, Q. Li, Z. Guo, *Advanced Energy Materials* **2019**, *9*, 1901795.
[33] F. Cao, W. Zeng, J. Zhu, J. Xiao, Z. Li, M. Li, R. Qin, T. Wang, J. Chen, X. Yi, J. Wang, S. Mu, *Small* **2022**, e2200713.
[34] J.-X. Huang, B. Li, B. Liu, B.-J. Liu, J.-B. Zhao, B. Ren, *J. Power Sources* **2016**, *310*, 85.
[35] V. Shanmugam, S. Natarajan, L. S. Lobo, A. Mathur, M. B. Sahana, G. Sundararajan, R. Gopalan, *J. Power Sources* **2021**, *515*, 230623.
[36] R. Baddour-Hadjean, J.-P. Pereira-Ramos, *Chem. Rev.* **2010**, *110*, 1278.
[37] S. Bhattacharya, A. R. Riahi, A. T. Alpas, *Carbon* **2014**, *77*, 99.
[38] D. Mohanty, S. Kalnaus, R. A. Meisner, K. J. Rhodes, J. Li, E. A. Payzant, D. L. Wood, C. Daniel, *J. Power Sources* **2013**, *229*, 239.
[39] J. Sun, C. Sheng, X. Cao, P. Wang, P. He, H. Yang, Z. Chang, X. Yue, H. Zhou, *Adv. Funct. Mater.* **2021**, *32*, 2110295.
[40] E. Castel, E. J. Berg, M. El Kazzi, P. Novák, C. Villevieille, *Chem. Mater.* **2014**, *26*, 5051.
[41] B. Strehle, K. Kleiner, R. Jung, F. Chesneau, M. Mendez, H. A. Gasteiger, M. Piana, *J. Electrochem. Soc.* **2017**, *164*, A400.
[42] W. Yang, T. P. Devereaux, *J. Power Sources* **2018**, *389*, 188.
[43] Z. Zhuo, Y.-s. Liu, J. Guo, Y.-d. Chuang, F. Pan, W. Yang, *The journal of physical chemistry letters* **2020**, *11*, 2618.
[44] R. A. House, U. Maitra, M. A. Perez-Osorio, J. G. Lozano, L. Jin, J. W. Somerville, L. C. Duda, A. Nag, A. Walters, K. J. Zhou, M. R. Roberts, P. G. Bruce, *Nature* **2020**, *577*, 502.
[45] Z. Zhuo, K. Dai, J. Wu, L. Zhang, N. Tamura, Y.-d. Chuang, J. Feng, J. Guo, Z.-x. Shen, G. Liu, F. Pan, W. Yang, *ACS Energy Letters* **2021**, *6*, 3417.
[46] K. Dai, J. Wu, Z. Zhuo, Q. Li, S. Sallis, J. Mao, G. Ai, C. Sun, Z. Li, W. E. Gent, W. C. Chueh, Y.-d. Chuang, R. Zeng, Z.-x. Shen, F. Pan, S. Yan, L. F. J. Piper, Z. Hussain, G. Liu, W. Yang, *Joule* **2019**, *3*, 518.